

Remote Sensing Exploration of Fullerene Bearing Shungite in Mangampet Baryte Mines, India

R. G. Rejith

National Institute for Interdisciplinary Science and Technology

M. Sundararajan (✉ rajanmsundar77@yahoo.com)

National Institute for Interdisciplinary Science and Technology

L. Gnanappazham

Indian Institute of Space Science and Technology

M. A. Mohammed-Aslam

Central University of Karnataka

Sarika Verma

Advanced Materials and Processes Research Institute

AK Srivastava

Advanced Materials and Processes Research Institute

Research Article

Keywords: Mangampet baryte mine, Fullerene, Landsat, ASTER, MTMF

Posted Date: March 3rd, 2021

DOI: <https://doi.org/10.21203/rs.3.rs-257269/v1>

License:   This work is licensed under a Creative Commons Attribution 4.0 International License.

[Read Full License](#)

Abstract

The fullerene (C_{60}) is economically significant due to its significant applications in diverse areas like nanochemistry, superconductivity, materials science, etc. The carbon allotrope fullerene C_{60} and C_{70} are identified within the thick sequence of black carbonaceous units belonging to the shungite suite of rock at the baryte mine, Mangampet, Andhra Pradesh. Since this is the first of its kind from India's geological material, the exploration of fullerenes enriched barytes from the mines at Mangampet in the Kadapa district is essential. In the present study, remote sensing techniques such as hyperspectral analysis followed by Mixture Tuned Matched Filtering (MTMF) and Support Vector Machine (SVM), and Principal Component Analysis (PCA) were used for exploring the presence of fullerene bearing baryte deposits in the Mangampet mine. The spectra measured for baryte samples were used as reference spectra for deriving true endmember from Landsat OLI and ASTER satellite data. The detailed characterisation of structure and chemistry of the baryte samples were carried out using techniques like Energy Dispersive X-ray Fluorescence (EDXRF), X-ray Powder Diffraction (XRD), X-ray Photoelectron Spectroscopy (XPS), and Fourier-Transform Infrared Spectroscopy (FTIR) techniques. The High-Performance Liquid Chromatography (HPLC) and Matrix-Assisted Laser Desorption/Ionization (MALDI) mass spectrometry analyses confirm fullerene presence in baryte deposits. The retention time at 11.783–11.822 min obtained from HPLC and high-intensity rate m/z at 720.178 obtained from MALDI spectra suggest fullerene in baryte mine deposits. The remote sensing exploration of fullerene bearing shungite suite of rocks in baryte mineral deposits of Mangampet mine has opened up new research areas for converting this material into value-added products.

1. Introduction

In 1985, a new form of carbon called fullerene (C_{60}) was first discovered, which consists of sixty carbon atoms situated at sixty vertices, all together forms 20 hexagons and 12 pentagons¹. It was also reported that C_{60} is considered the most symmetric molecule with 120 symmetry operations possible due to the unique structure formed by the arrangement of carbon atoms as 20 hexagons and 12 pentagons². Altogether it includes a hollow spherical cage-like structure with the unique ability to trap particles of size even in nanometers. The unique physical and chemical properties of fullerene have opened up tremendous usages in various essential areas like solar cells³, semiconductor (OSC) materials⁴, photocatalysts⁵, organic optoelectronic applications^{6,7}, and biological and Biomedical applications respectively⁸⁻¹⁰. Buseck et al. reported the occurrence of naturally occurring fullerene in the shungite rocks of Karelea¹¹. Later in India, fullerene bearing shungite rocks were discovered in the Mangampet baryte mine located in Kadapa District, Andhra Pradesh¹². It also states that the interlayered thick black colored slates of carbonaceous shale present in baryte mines confirm that shungite suit of rocks have a composition of carbon-hydrogen-sulphur. Further, Inductively Coupled Plasma Mass Spectrometry (ICP-MS) shows the traces of Be, Co, Ga, Ge, Y, Zr, etc. The laser desorption/ionization mass spectrometry gives the main peaks near $m/z = 720$ amu and 840 amu indicating the presence of C_{60} and C_{70} . It is

estimated to about 74 million tonnes of reserves in Mangampet mine, which is known to be the largest in the World. The Andhra Pradesh Mineral Development Corporation Limited (APMDC) is engaged in the mining of barytes, and baryte mining contributes more than 95% of the turnover. The fullerene-bearing shungite deposits along with white shale are left as mine dumps. So the need for converting this material into value-added products and marketing is the main concern of the scientific community.

Remote sensing applications of geology and mineral exploration start with the advent of Landsat multispectral satellite imagery, which was mainly used to delineate potential mineral occurrences related to hydrothermal alteration zones. The band ratio, principal component analysis (PCA), and spectral angle mapper (SAM) applied to Landsat ETM+ and OLI data successfully detect alteration minerals associated with porphyry copper mineralization¹³. Later, shortwave infrared bands of ASTER and Landsat 8 were used to successfully extract the solid information about clays and iron oxide minerals. The techniques such as Spectral Angle Mapping (SAM), Mixture Tuned Match Filtering (MTMF), Crosta technique, and Spectral Feature Fitting (Hewson and Cudahy 2010, Pour and Hashim 2014) were used. RGB composites, Spectral Angle Mapping (SAM), Color composites of PC bands derived from Landsat ETM+, ASTER, and Sentinel-2A discriminates granitic intrusions associated with copper mineralization¹⁴, alteration zones related to igneous bedrock¹⁵, lithological units¹⁶, and rock units associated with ophiolite complex¹⁷. The advent of hyperspectral imagery, such as Airborne Visible/Infrared Imaging Spectrometer-Next Generation (AVIRIS-NG) made a significant mineral mapping breakthrough. The MTMF, Spectral Feature Fitting (SFF), SAM, and Spectral Information Divergence (SID) applied to AVIRIS-NG and Hyperion successfully maps hydrothermal alteration minerals¹⁸⁻²⁰. A wide range of mineral types ranging from copper-gold mineralization, chromite occurrences, mafic-ultramafic rocks, hydrothermal alteration minerals, beach minerals were successfully demarcated using remote sensing data and techniques. Apart from band ratio, spectral indices and PCA, advanced image classification algorithms including Machine Learning, Random Forest, and Artificial neural networks were also used for mapping lithology²¹, gold mineralization²², Cu potential areas²³, etc. In mineral exploration studies, structural and geochemical characterisation is fundamental to confirm the mineral type, grain size, etc. The X-ray diffraction (XRD) spectra of clays in rock samples were collected from the region where the hydrothermal alteration mapping was carried out using Landsat and ASTER^{13,24}. The XRD and XRF techniques were used to confirm the iron ore deposits mapped using Maximum Likelihood supervised classification of LandsatTM+ data²⁵. The XRF analysis confirms the presence of gold collected from alteration zones (gossanic ridges) mapped using spectral band rationing techniques applied to Landsat 8 OLI image and thereby validated the importance of remote sensing exploration²⁶.

As follow-up to our previous study on beach sediments, we tried to investigate baryte deposits in Mangampet mine of Andhra Pradesh, India using hyperspectral analysis followed by image classification using MTMF and SVM. The reference spectra developed from the laboratory spectra is used for deriving the true endmembers from ASTER and Landsat data. The validation of fullerene bearing baryte deposits was also carried out using ED-XRF, XRD, XPS, FTIR, HPLC, and MALDI analyses.

2. Study Area

The Mangampet baryte mine is located in the geographic location of 14°1'46.21"N latitude and 79°18'52.34"E longitude in the southern part of Kadapa District of state Andhra Pradesh in India (Fig. 1 and Fig. 2). The fullerene bearing shungite rocks were discovered first in this area by²⁷. The interlayered thick black colored slates of carbonaceous shale that exist in baryte mines are confirmed that of shungite suite of rocks by carbon-hydrogen-sulphur composition. It is estimated to about 74 million tonnes of reserves known to be the largest in the World. The present study area belongs to the structurally configured "pull apart" Proterozoic Cuddapah Basin, and lithology is dominated by quartzites, shales, dolomites, and chert intercalations, limestone, dolerites, and basalts.

The rock strata of Cuddapah Supergroup consists of arenaceous and argillaceous sediments overlain by carbonate sediments associated with Kurnool Group and the upper part covered by clastics. Barytes mineralization is attributed to the hydrothermal solution and contact metamorphism in contact zones of dolomites with the igneous still intrusive. The bya zone of lapilli baryte is considered one of the economically essential deposits. It is overlined by granular baryte beds seen in the upper Carbonaceous tuff zone of Cuddapah Supergroup. It has also occurred in association with copper mineralization zones of pyrite, chalcopyrite, azurite, etc. The Proterozoic Cuddapah Basin with a crescent-shaped structure is formed over the high-grade Archaean crust of the Eastern Dharwar Craton. The sub-basins are formed by large dolerite dykes. The basin is filled with strategic minerals like baryte, asbestos, limestone, phosphorites, uranium, and diamond²⁸.

3. Materials And Methods

The flowsheet showing the detailed methodology is shown in Fig. 3. The methodology includes (i) Satellite data and pre-processing, (ii) Collection of reference spectra and extraction of target endmembers, (iii) Image Classification using Mixture Tuned Matched Filtering (MTMF) and Support Vector Machine (SVM), (iv) Band rationing of PC bands, and (v) Instrumentation.

3.1. Satellite data and Pre-Processing

Cloud free datasets of Landsat 8 and ASTER L1B scenes acquired on 2018-05-06 and 2002-12-21 were used for extracting the target endmembers. The Landsat 8 consists of two sensors such as Operational Land Imager (OLI) and the Thermal Infrared Sensor (TIRS). The OLI consists of 9 bands, and TIRS consists of 2 bands. The ASTER data with 14 bands are mainly designed to measure the reflected radiations in VNIR (3 bands) in the range 0.52 to 0.86 μm , SWIR (6 bands) in the range 1.6 to 2.43 μm and also the emitted thermal radiations (5 bands) in the range 8.125 to 11.65 μm (Abrams and Hook 1995). The geometric correction, reflectance calibration, and atmospheric corrections were carried out using Crosstalk correction software (for SWIR bands of ASTER data) and FLAASH (Fast line-of-sight Atmospheric Analysis of Spectral Hypercubes) modules²⁹⁻³¹. In the present study, hyperspectral data analysis was carried out to bands 1–5 and band 7 of Landsat 8 whereas in ASTER the bands 1–9 are

used. Integration of hyperspectral analysis techniques and multispectral data facilitate accurate mapping of mineral deposits^{29,30,32,33}.

3.2. Collection of reference spectra and Extraction of target endmembers

The hyperspectral data analysis consists of six processes such as (i) Atmospheric correction and extraction of reflectance values, (ii) spectral data reduction and noise reduction, (iii) spatial data reduction and pure pixel extraction, (iv) endmember extraction, (v) identification of mineral classes, and (vi) satellite image classification^{33,34}. All these procedures were carried out using the Advanced spectral Analysis (ASA) module available in the software package of ENVI version 5.1. Minimum noise fraction (MNF) is a linear transformation technique applied to reduce the spectral bands of calibrated reflectance dataset³⁵. The eigen values calculated from the noise statistics of input data are used to select the MNF bands with maximum variance. The Pixel purity index (PPI) generates a new PPI image showing spectrally pure pixels as bright pixels. The n-d visualizer helps to extract the target endmembers from the pixel clouds of pure pixels. Here n-D scatter plot of pure pixels are rotated and visualized in different directions and angles for isolating target endmembers. The spectral matching techniques such as Spectral Feature Fitting (SFF), Spectral Angle Mapper (SAM), and Binary Encoding (BE) were used to identify the true end members of target minerals³⁰.

Representative samples of baryte were collected from the field, and their laboratory spectrum was measured using ASD Fieldspec® 3 spectroradiometer^{29,36,37}. The pre-processed data were imported to the ENVI software for developing the reference spectrum.

3.3. Image Classification using MTMF and SVM

The true endmembers derived from the satellite data are mapped using the Mixture Tuned Matched Filtering (MTMF) classification technique. MTMF is a partial unmixing process that is a useful image processing technique for mapping minerals that shows remarkable differences from their background^{38,39}. It highlights the spectral response of the mineral of interest by suppressing background response⁴⁰. It integrates two methods, such as matched filter (MF) method to estimate the abundance and linear spectral mixing theory (MT) to reject false positives, therefore possesses the advantages of two ways⁴¹. No prior knowledge regarding the background spectral signature is required for the processing (matched filter (MF)). The linear combination of individual components in each pixel gives a spectral signature for that particular pixel (linear spectral mixing theory). Apart from this, it reduces individual methods' weakness also^{42,43}. High value for MF (close to 1) and low value for infeasibility(close to 0) represents closer matches and indicates a high probability for mineral occurrences³⁹. The MTMF shows better results for mapping magnetite, pyrite, kaolin, etc., and alteration minerals from Landsat ETM+, Landsat 8, and ASTER data^{33,43}.

Support Vector Machine (SVM) is a non-parametric supervised classification technique based on statistical learning theory. It is used for classifying multispectral and hyperspectral datasets using data points from the training set recorded during the field survey. Here the algorithm uses an optimal hyperplane that separates two classes by maximizing the distance between them. The levels or data points that lie very close to the hyperplane are called support vectors, and the distance between these support vectors to the boundary of separation is termed as margin. The hyperplane maximizes the margin's width using the support vectors results in the classification of pixels in the image⁴⁴. Over the years, SVM has been successfully used for mapping Au deposits⁴⁵, Chromite mineralization⁴⁶, and porphyry-Cu deposits⁴⁷ from satellite data of varying resolutions. Different kernels are used to convert the nonlinear space to linear space of higher dimension, which effectively defines the optimal hyperplane in nonlinear classifications. The radial basis function (RBF) is the most used kernel for lithological mapping^{16,21,46}. In the present study, the SVM classification of Landsat 8 data is used for demarcating the boundaries of shungite rocks using the training pixels collected by ground truth and geological map. The ENVI software module is used for executing the SVM algorithm. The Kernel type used is radial basis function (RBF) with a penalty parameter of 100. The FLAASH calibrated Landsat 8 data have six bands, so its gamma value is 0.167.

3.4. Band rationing of PC bands

Principal component analysis (PCA) is a multivariate statistical method. The correlated multivariate datasets are linearly transformed into uncorrelated image bands called Principle bands or PC bands. During the transformation, the data variance is maximized due to the rotation of orthogonal axes that are newly formed and have the origin at the data mean⁴⁸. Here the PCA generates the same number of PC bands as that of input satellite data. The first PC band shows the highest data variance, which can be used for further processing, leaving the bands with very low data variance, reducing the spectral redundancy in multiband datasets⁴⁹. Since the PC bands are uncorrelated, the color composites and band rationing of PC bands provide better discrimination of mineral occurrences on the surface of the earth. The RGB color composite of PC bands generated from Landsat and ASTER data was also used for delineating the shungite rocks in Mangampet.

3.5. Instrumentation

The X-ray diffraction (XRD) peaks of the baryte samples were taken using PANalytical X'Pert Pro diffractometer. The major oxides and trace elements present in the samples are determined using the Pan Analytical Epsilon 3 ED-XRF instrument with Omnion software. The Attenuated Total Reflection-Fourier Transform Infrared (ATR-FTIR) spectra were taken using PerkinElmer Spectrum Two FT-IR Spectrometer equipped with Universal ATR. The chemical state of major elements was analysed using the XPS analysis (Multilab 2000,.). HPLC and MALDI analyses were carried out for confirming the presence of fullerene in baryte samples. The powdered samples were demineralized using 1:1 of 37% HCL and 48% HF⁵⁰. After demineralization, toluene is added, sonicated, and filtered through 0.2µm PTFE filter paper. The solution is used for HPLC and MALDI analyses. The HPMLC analyses was carried out for baryte samples (two sets

of 0.5mg/ml) and compared with the standard fullerene (0.1, 0.2, 0.3, 0.4, and 0.5 mg/ml). The HPLC was carried out using Shimadzu Prominence UFLC C-18 column. The mobile phase used for the present study is 40:60 toluene: methanol mixture⁵⁰.

4. Results And Discussion

4.1. Mapping of baryte deposits

The reflectance calibrated and FLAASH atmospherically corrected nine VNIR-SWIR bands of ASTER, and seven VNIR-SWIR bands of Landsat imageries were used for the study.

The MNF transformation eliminates the least informative and noisy bands from the satellite data. The PPI image showing too pure pixels as bright ones are generated using a threshold value of 3 and 100 iterations. The endmembers generated using 2-D plots of MNF bands were compared with reference spectra using spectral matching techniques, and true endmembers of shungite rocks were identified. The scores of SAM, SFF, and BE correspond to the highest degree of the match were shown in Table 1, and the corresponding plots of relative reflectance are shown in Fig. 4. On comparing with the reference spectra, one end member out of six extracted from the Landsat data shows the maximum score of 2.797. In the case of ASTER data, one out of eight endmembers shows the maximum similarity with reference spectra with a score of 2.050. Figure 5 and Fig. 6 show the MTMF and SVM classified images showing shungite deposits of baryte mine in red color. The MTMF gives the most satisfying results compared to others for mapping a particular target rather than other materials in the scene⁴³. The employed techniques show good consistency with the geological map by showing clear demarcation of shungite rocks and the mine wastes dumped around the mine. The results suggest the potential of the proposed methodology for the clear prospecting of mineral occurrences in the study area, which facilitates sustainable and profitable mining of these strategic minerals.

Table 1
Results of spectral matching technique

Satellite data	Date of acquisition	SAM	SFF	BE	Score
Landsat 8	2018-05-06	0.823	0.974	1	2.797
ASTER	2002-12-21	0.583	0.689	0.778	2.050

The eigen vectors indicating the contribution of satellite data bands corresponding to their PC bands are shown in Table 2 and Table 3. Table 2 represents the PC bands of Landsat data (six bands), and Table 3 corresponds to ASTER data (nine bands). Table 4 gives the percentage of total variance or percentage of information content available with each band. The results show that lower PC bands obtained for both Landsat and ASTER store the maximum information compared to higher bands. The highly informative PC bands PC1 – PC3 of Landsat and ASTER hold 98.346% and 98.290% of total information that are significant and could be used successfully for identifying the shungite rocks. The RGB color composite of

principal components PC1, PC2, and PC3 of Landsat and ASTER were employed to restrict the shungite rock units from the surrounding lithological units and land use/land cover features. Figure 7 and Fig. 8 show the RGB color composite of PC bands generated using Landsat and ASTER. It is clearly observed that this RGB composite gives higher contrast and color saturation than standard data bands, which enables better visual interpretation of shungite rock units. The PC1 derived from Landsat and ASTER shows the total variance of 51.159% and 83.637% enhances the shungite rocks in bright pixels. The PC2 derived from Landsat and ASTER shows the total variance of 42.831% and 9.801% shows the opposite contribution by improving the shungite rocks in dark pixels. As illustrated in Fig. 7(a) and Fig. 8(a), the shungite rocks and mine wastes dumped around the mine are characterised by pink-amaranth color, which shows better contrast and clear boundaries, which is easy to distinguish from surrounding features. The last PC bands, such as PC4- PC9 and PC4-PC6 of ASTER and Landsat are noise dominant images which do not discriminate the shungite rocks from the surrounding features. These higher PC bands of Landsat (PC4-PC6) and ASTER (PC4-PC9) represent low information and low data variability removed for further processing.

Table 2
Contribution of Landsat bands to the corresponding PC bands

Principal components	Band 1	Band 2	Band 3	Band 4	Band 5	Band 6
PC 1	0.207	0.210	0.167	0.281	-0.898	0.007
PC 2	0.260	0.292	0.418	0.655	0.414	0.270
PC 3	0.565	0.511	0.190	-0.518	0.120	-0.318
PC 4	0.173	0.152	-0.243	-0.310	-0.060	0.888
PC 5	-0.259	-0.249	0.838	-0.355	-0.072	0.194
PC 6	-0.688	0.724	-0.012	-0.037	-0.003	-0.006

Table 3
Contribution of ASTER bands to the corresponding PC bands

Principal components	Band 1	Band 2	Band 3	Band 4	Band 5	Band 6	Band 7	Band 8	Band 9
PC 1	-0.138	-0.297	-0.142	-0.367	-0.315	-0.331	-0.347	-0.374	-0.519
PC 2	-0.351	-0.508	0.699	0.333	0.043	0.067	0.025	-0.028	-0.107
PC 3	0.473	0.504	0.644	-0.104	-0.123	-0.115	-0.135	-0.138	-0.178
PC 4	0.006	0.258	-0.252	0.695	0.095	0.092	0.016	-0.156	-0.587
PC 5	-0.785	0.566	0.102	-0.161	-0.021	-0.125	0.066	0.077	-0.036
PC 6	0.087	-0.092	0.048	-0.388	0.261	0.193	0.304	0.542	-0.583
PC 7	0.055	-0.038	-0.009	0.198	0.333	-0.738	-0.320	0.444	0.033
PC 8	-0.025	0.011	0.026	-0.209	0.829	0.018	-0.031	-0.516	0.018
PC 9	-0.082	0.058	-0.001	-0.030	0.092	0.516	-0.813	0.232	0.002

Table 4
Results of PCA showing the percentage of information content of PC bands

ASTER PC	Variance (%)	Landsat PC	Variance (%)
PC 1	83.637	PC 1	51.159
PC 2	9.801	PC 2	42.831
PC 3	4.908	PC 3	4.300
PC 4	0.769	PC 4	1.459
PC 5	0.439	PC 5	0.213
PC 6	0.188	PC 6	0.039
PC 7	0.104		
PC 8	0.088		
PC 9	0.065		

4.2. Characterisation of baryte

Baryte has an orthorhombic structure with sulphur in tetrahedral coordination with oxygen and barium in 12-fold coordination. The XRD results are shown in Fig. 9(a). The XRD of the collected samples shows characteristic diffraction peaks of baryte (BaSO_4)^{51,52}. The bulk geochemistry of baryte mineral analyzed

using ED-XRF is shown in Table 5. The result shows that SO_3 (36.304%) is the major compound followed by BaO (33.959%). The decreasing order of compounds present in the baryte mineral is $\text{SO}_3 > \text{BaO} > \text{Fe}_2\text{O}_3 > \text{SiO}_2 > \text{Al}_2\text{O}_3 > \text{P}_2\text{O}_5 > \text{K}_2\text{O} > \text{TiO}_2 > \text{CaO} > \text{Eu}_2\text{O}_3 > \text{SrO} > \text{As}_2\text{O}_3 > \text{CdO} > \text{CuO} > \text{ZnO} > \text{ZrO}_2 > \text{Rb}_2\text{O}$. The ATR-FTIR spectra of baryte mineral shown in Fig. 9(b). The bands appear at 1076 cm^{-1} and 980 cm^{-1} belong to symmetrical vibrations of sulphate, while the peak at 605 cm^{-1} belongs to the out-of-plane bending vibration of sulphate^{53,54}. The peak observed at 1431 cm^{-1} corresponds to the carbonate's stretching, which confirms carbonates' presence⁵⁵. ATR-FTIR spectra of the sample confirm the presence of baryte mineral. The XPS results of the baryte are shown in Fig. 10 (a-d). The Ba3d shows two of $\text{Ba}3d^{5/2}$ and $\text{Ba}3d^{3/2}$ at binding energies of 780.44 and 795.84eV. The binding of S2p and O1s are 168.94eV and 531.95eV^{56,57}.

Table 5
ED-XRF of barite mineral

Compound	Concentration
SO_3 (%)	36.304
BaO (%)	33.959
Fe_2O_3 (%)	20.44
SiO_2 (%)	5.644
Al_2O_3 (%)	1.18
P_2O_5 (%)	0.725
K_2O (%)	0.478
TiO_2 (%)	0.34
CaO (%)	0.233
Eu_2O_3 (%)	0.207
SrO (%)	0.195
As_2O_3 (%)	0.138
CdO (%)	0.136
CuO (ppm)	110.9
ZnO (ppm)	43.2
ZrO_2 (ppm)	32.9
Rb_2O (ppm)	14

4.3. Confirmation of fullerene

HPLC analysis results were carried out for standards, and the baryte samples, which are depicted in Fig. 11(a1-a5) and Fig. 11(b1-b2). In both samples, the retention time at 11.783–11.822 min corresponds to the presence of C₆₀^{58,59}. Thus the HPLC results clearly suggest the presence of fullerene in baryte mine deposits. The MALDI spectra of fullerene standard and baryte samples are shown in Fig. 12 (a-b). The characteristic high intensity at m/z at 720.855 and 720.178 of fullerene standard and baryte samples indicate the fullerenes' Minimal fragmentation⁶⁰. Both HPLC and MALDI confirm the presence of fullerene in Mangampet baryte deposits.

5. Conclusion

The critical applications of fullerene in diverse fields make the shungite rocks of baryte a strategic mineral of high economic value. Remote sensing exploration of these strategic minerals was successfully achieved using hyperspectral data analysis followed by MTMF and SVM classification algorithms and Principle component analysis. The true endmembers denote the shungite rock units were successfully delineated using laboratory-derived reference spectra. The results show a strong correlation with the geological map and ground truth data. Moreover, detailed characterisation, MALDI, and HPLC carried out to the samples confirm the presence of fullerene bearing baryte deposits. Integrated remote sensing exploration and Geochemical characterisation techniques facilitates an eco-friendly and sustainable mining of strategic mineral deposits.

Declarations

Acknowledgements

The first author thanks the DST-INSPIRE Division, Department of Science & Technology (DST), Government of India for providing the INSPIRE fellowship. The authors thank Mr. Renjith. R. A for the great help in carrying out the HPLC and MALDI analyses. The authors also thank the Director, CSIR-National Institute for Interdisciplinary Science and Technology (CSIR-NIIST), Trivandrum, Kerala, India for extending the laboratory facilities.

Author contributions

M.S. involved in overall Project design, concept and coordination. RGR carried out the analysis and wrote the manuscript. LG, MAM, SV, and AKS discussed the results, and revised the manuscript. LG advised at every stage and reviewed the manuscript.

Additional Information

The author(s) declare no competing interests.

References

1. Kroto, H. W., Heath, J. R., O'Brien, S. C., Curl, R. F. & Smalley, R. E. *Buckminsterfullerene*. *Nature* **318**, C60, 162–163 (1985).
2. Diwan, P. & Bharadwaj, A. *The nanoscope: encyclopedia of nanoscience and nanotechnology* (Pentagon Press, 2005).
3. Sorrentino, R., Kozma, E., Luzzati, S. & Po, R. Interlayers for non-fullerene based polymer solar cells: distinctive features and challenges. *Energy Environ. Sci.* <https://doi.org/10.1039/d0ee02503h> (2021).
4. Halaby, S. *et al.* Microcrystal Electron Diffraction for Molecular Design of Functional Non-Fullerene Acceptor Structures. *Chem. Mater.* *acs.chemmater.0c04111*. <https://doi.org/10.1021/acs.chemmater.0c04111> (2021).
5. Jozeliūnaitė, A., Valčekas, D. & Orentas, E. Fullerene soot and a fullerene nanodispersion as recyclable heterogeneous off-the-shelf photocatalysts. *RSC Adv.* **11**, 4104–4111 (2021).
6. Cravino, A. & Sariciftci, N. S. Double-cable polymers for fullerene based organic optoelectronic applications. *Journal of Materials Chemistry*. <https://doi.org/10.1039/b201558g> (2002).
7. Yadav, B. C. & Kumar, R. Structure, properties and applications of fullerenes. *Int. J. Nanotechnol. Appl. ISSN.* **2**, 15–24 (2008).
8. Conyers, J. Biomedical applications of functionalized fullerene-based nanomaterials. *Int. J. Nanomedicine.* **261**, <https://doi.org/10.2147/IJN.S5964> (2009).
9. Pinheiro, F. G. *et al.* Eugenol mitigated acute lung but not spermatotoxicity of C60 fullerene emulsion in mice. *Environ. Pollut.* <https://doi.org/10.1016/j.envpol.2020.116188> (2021).
10. Sugikawa, K., Masuda, K., Kozawa, K., Kawasaki, R. & Ikeda, A. Fullerene–porphyrin hybrid nanoparticles that generate activated oxygen by photoirradiation. *RSC Adv.* **11**, 1564–1568 (2021).
11. Buseck, P. R., Tsipursky, S. J. & Hettich, R. Fullerenes from the geological environment. *Science (80-)*. (1992). doi:10.1126/science.257.5067.215
12. Misra, K. S. *et al.* Occurrence of fullerene bearing shungite suite rock in Mangampeta area, Cuddapah District, Andhra Pradesh. *J. Geol. Soc. India* (2007).
13. Masoumi, F., Eslamkish, T., Honarmand, M. & Abkar, A. A Comparative Study of Landsat-7 and Landsat-8 Data Using Image Processing Methods for Hydrothermal Alteration Mapping. *Resour. Geol.* **67**, 72–88 (2017).
14. Liu, L. *et al.* Targeting Mineral Resources with Remote Sensing and Field Data in the Xiemisitai Area, West Junggar, Xinjiang, China. *Remote Sens.* **5**, 3156–3171 (2013).
15. Mahmoudishadi, S., Malian, A. & Hosseinali, F. Comparing independent component analysis with principle component analysis in detecting alterations of porphyry copper deposit (case study: Ardestan area, Central Iran). in *International Archives of the Photogrammetry, Remote Sensing and Spatial Information Sciences - ISPRS Archives* (2017). doi:10.5194/isprs-archives-XLII-4-W4-161-2017

16. Gasmi, A., Gomez, C., Zouari, H., Masse, A. & Ducrot, D. PCA and SVM as geo-computational methods for geological mapping in the southern of Tunisia, using ASTER remote sensing data set. *Arab. J. Geosci.* **9**, 753 (2016).
17. Ge, W., Cheng, Q., Tang, Y., Jing, L. & Gao, C. Lithological Classification Using Sentinel-2A Data in the Shibanjing Ophiolite Complex in Inner Mongolia, China. *Remote Sens.* **10**, 638 (2018).
18. Kumar, C., Chatterjee, S. & Oommen, T. Mapping hydrothermal alteration minerals using high-resolution AVIRIS-NG hyperspectral data in the Hutti-Maski gold deposit area, India. *Int. J. Remote Sens.* <https://doi.org/10.1080/01431161.2019.1648906> (2020).
19. Tripathi, M. K. & Govil, H. Evaluation of AVIRIS-NG hyperspectral images for mineral identification and mapping. *Heliyon.* <https://doi.org/10.1016/j.heliyon.2019.e02931> (2019).
20. Kruse, F. A., Boardman, J. W. & Huntington, J. F. Comparison of airborne hyperspectral data and eo-1 hyperion for mineral mapping. *IEEE Trans. Geosci. Remote Sens.* **41**, 1388–1400 (2003).
21. Bachri, I., Hakdaoui, M., Raji, M., Teodoro, A. C. & Benbouziane, A. Machine Learning Algorithms for Automatic Lithological Mapping Using Remote Sensing Data: A Case Study from Souk Arbaa Sahel, Sidi Ifni Inlier, Western Anti-Atlas, Morocco. *ISPRS Int. J. Geo-Information.* **8**, 248 (2019).
22. Rigol-Sanchez, J. P., Chica-Olmo, M. & Abarca-Hernandez, F. Artificial neural networks as a tool for mineral potential mapping with GIS. *Int. J. Remote Sens.* **24**, 1151–1156 (2003).
23. Sun, T., Chen, F., Zhong, L., Liu, W. & Wang, Y. GIS-based mineral prospectivity mapping using machine learning methods: A case study from Tongling ore district, eastern China. *Ore Geol. Rev.* **109**, 26–49 (2019).
24. Bolouki, S. M., Ramazi, H. R., Maghsoudi, A., Pour, A. B. & Sohrabi, G. A remote sensing-based application of bayesian networks for epithermal gold potential mapping in Ahar-Arasbaran area, NW Iran. *Remote Sens.* <https://doi.org/10.3390/rs12010105> (2020).
25. Abulghasem, Y. A., Akhir, J. B. M., Hassan, W. F. W., Samsudin, A. R. & Youshah, B. M. The use of remote sensing technology in geological investigation and mineral detection in Wadi shati, Libya. *Electron. J. Geotech. Eng.* (2012).
26. Zeinelabdein, K. A. E., Halim, A., Nadi, H. & El The use of Landsat 8 OLI image for the delineation of gossanic ridges in the Red Sea Hills of NE Sudan. *Am. J. Earth Sci.* **1**, 62–67 (2014).
27. Modabberi, S., Ahmadi, A. & Tangestani, M. H. Sub-pixel mapping of alunite and jarosite using ASTER data; a case study from north of Semnan, north central Iran. *Ore Geol. Rev.* **80**, 429–436 (2017).
28. Nageswara Rao, M., Dikshitulu, G. R., Desapati, T. & Krishnan, S. Mir Azam Ali. A STRATEGIC PLACER MINERAL DEPOSIT ALONG TANDAVA-VARAHA RIVER GOASTAL AREA, VISAKHAPATNAM DISTRICT, ANDHRA PRADESH. *JOAMS* 7(2001).
29. Rejith, R. G., Sundararajan, M., Gnanappazham, L. & Loveson, V. J. Satellite-based spectral mapping (ASTER and landsat data) of mineralogical signatures of beach sediments: a precursor insight. *Geocarto Int.* 1–24 <https://doi.org/10.1080/10106049.2020.1750061> (2020).

30. Rejith, R. G., Sundararajan, M. & Mohammed-Aslam, M. A. S., V. & Remote sensing for exploring heavy mineral deposits: a case study of Chavara and Manavalakurichi deposits, southwest coast of India. in *Remote Sensing of Ocean and Coastal Environments 1st Edition* 177–188 (Elsevier, 2020).
31. Rejith, R. G. & Sundararajan, M. Mapping of mafic-ultramafic rock units in late Archean Bhavani Complex, southern India using ASTER thermal bands. in *Shear Zones and Crustal Blocks of Southern India* 34–40(2018).
32. Yousefi, T., Aliyari, F., Abedini, A. & Calagari, A. A. Integrating geologic and Landsat-8 and ASTER remote sensing data for gold exploration: a case study from Zarshuran Carlin-type gold deposit, NW Iran. *Arab. J. Geosci.* **11**, 482 (2018).
33. Pal, S. K., Majumdar, T. J., Bhattacharya, A. K. & Bhattacharyya, R. Utilization of Landsat ETM + data for mineral-occurrences mapping over Dalma and Dhanjori, Jharkhand, India: an Advanced Spectral Analysis approach. *Int. J. Remote Sens.* **32**, 4023–4040 (2011).
34. Rajan Girija, R. & Mayappan, S. Mapping of mineral resources and lithological units: a review of remote sensing techniques. *International Journal of Image and Data Fusion.* **10**, 79–106 (2019).
35. Green, A. A., Berman, M., Switzer, P. & Craig, M. D. A Transformation for Ordering Multispectral Data in Terms of Image Quality with Implications for Noise Removal. *IEEE Trans. Geosci. Remote Sens.* <https://doi.org/10.1109/36.3001> (1988).
36. Prasad, K. A., Gnanappazham, L., Selvam, V., Ramasubramanian, R. & Kar, C. S. Developing a spectral library of mangrove species of Indian east coast using field spectroscopy. *Geocarto Int.* **30**, 580–599 (2015).
37. Prasad, K. A. & Gnanappazham, L. Discrimination of mangrove species of Rhizophoraceae using laboratory spectral signatures. in 2014 *IEEE Geoscience and Remote Sensing Symposium* 2906–2909 (IEEE, 2014). doi:10.1109/IGARSS.2014.6947084
38. Boardman, J. W. Leveraging the high dimensionality of AVIRIS data for improved sub-pixel target unmixing and rejection of false positives: mixture tuned matched filtering. 7th JPL Airborne Earth Sci. Work.(1998).
39. Goodarzi Mehr, S., Ahadnejad, V., Abbaspour, R. A. & Hamzeh, M. Using the mixture-tuned matched filtering method for lithological mapping with Landsat TM5 images. *Int. J. Remote Sens.* <https://doi.org/10.1080/01431161.2013.853144> (2013).
40. Parker Williams, A. & Hunt, E. R. Estimation of leafy spurge cover from hyperspectral imagery using mixture tuned matched filtering. *Remote Sens. Environ.* [https://doi.org/10.1016/S0034-4257\(02\)00061-5](https://doi.org/10.1016/S0034-4257(02)00061-5) (2002).
41. Mundt, J. T., Streutker, D. R. & Glenn, N. F. Partial unmixing of hyperspectral imagery: Theory and methods. *Am. Soc. Photogramm. Remote Sens. - ASPRS Annu. Conf. 2007 Identifying Geospatial Solut.* (2007).
42. Boardman, J. W., Kruse, F. & Green, R. O. Mapping target signatures via partial unmixing of AVIRIS data. *Summ. JPL Airborne Earth Sci. Work.*(1995).

43. Hosseinjani, M. & Tangestani, M. H. Mapping alteration minerals using sub-pixel unmixing of aster data in the sarduiyeh area, se kerman, iran. *Int. J. Digit. Earth*. <https://doi.org/10.1080/17538947.2010.550937> (2011).
44. Oommen, T. *et al.* An Objective Analysis of Support Vector Machine Based Classification for Remote Sensing. *Math. Geosci.* **40**, 409–424 (2008).
45. Zuo, R. & Carranza, E. J. M. Support vector machine: A tool for mapping mineral prospectivity. *Comput. Geosci.* **37**, 1967–1975 (2011).
46. Othman, A. & Gloaguen, R. Improving Lithological Mapping by SVM Classification of Spectral and Morphological Features: The Discovery of a New Chromite Body in the Mawat Ophiolite Complex (Kurdistan, NE Iraq). *Remote Sens.* **6**, 6867–6896 (2014).
47. Abedi, M., Norouzi, G. H. & Bahroudi, A. Support vector machine for multi-classification of mineral prospectivity areas. *Comput. Geosci.* **46**, 272–283 (2012).
48. Pour, A. B. & Hashim, M. Spectral transformation of ASTER data and the discrimination of hydrothermal alteration minerals in a semi-arid region, SE Iran. *Int. J. Phys. Sci.* **6**, 2037–2059 (2011).
49. Chuvieco, E. & Huete, A. Fundamentals of satellite remote sensing. *Fundamentals of Satellite Remote Sensing*. <https://doi.org/10.1201/b18954> (2009).
50. Heymann, D., Korochantsev, A., Nazarov, M. A. & Smit, J. Search for fullerenes C60 and C70 in Cretaceous–Tertiary boundary sediments from Turkmenistan, Kazakhstan, Georgia, Austria, and Denmark. *Cretac. Res.* **17**, 367–380 (1996).
51. Al-Awad, M. N. J. & Al-Qasabi, A. O. Characterization and Testing of Saudi Barite for Potential Use in Drilling Operations. *J. King Saud Univ. - Eng. Sci.* **13**, 287–298 (2001).
52. Ansari, T. M., Marr, I. L. & Coats, A. M. Characterisation of mineralogical forms of barium and trace heavy metal impurities in commercial barytes by EPMA, XRD and ICP-MS. *Journal of Environmental Monitoring*. <https://doi.org/10.1039/b007943j> (2001).
53. Chen, R., Zhou, J., Xu, B. & Meng, X. Preparation of TiO₂–BaSO₄ composite microparticles and their photocatalytic activity. *Chem. Eng. J.* **218**, 24–31 (2013).
54. Nandakumar, N. & Kurian, P. Chemosynthesis of monodispersed porous BaSO₄ nano powder by polymeric template process and its characterisation. *Powder Technol.* <https://doi.org/10.1016/j.powtec.2012.02.022> (2012).
55. Larachi, N., Bali, A., Ould Hamou, M. & Bensaadi, S. Recovery of lead and barite from the abandoned Ichmoul mine wastes in Algeria. *Environ. Earth Sci.* <https://doi.org/10.1007/s12665-019-8593-5> (2019).
56. Zhou, H., Wang, M., Ding, H. & Du, G. Preparation and Characterization of Barite/TiO₂ Composite Particles. *Adv. Mater. Sci. Eng.* **2015**, 1–8 (2015).
57. Schmitz, P. J. Characterization of the Surface of BaSO₄ Powder by XPS. *Surf. Sci. Spectra.* **8**, 195–199 (2001).

58. Víték, P. *et al.* Optimizing Conditions for Ultrasound Extraction of Fullerenes from Coal Matrices. *Fullerenes, Nanotub. Carbon Nanostructures*. **17**, 109–122 (2009).
59. Jehlička, J., Svatoš, A., Frank, O. & Uhlík, F. Evidence for fullerenes in solid bitumen from pillow lavas of Proterozoic age from Mítov (Bohemian Massif, Czech Republic). *Geochim. Cosmochim. Acta*. [https://doi.org/10.1016/S0016-7037\(00\)01404-7](https://doi.org/10.1016/S0016-7037(00)01404-7) (2003).
60. Deacon, G. B. *et al.* Fullerene matrices in the MALDI-TOF mass spectroscopic characterisation of organometallic compounds. *J. Organomet. Chem.* **751**, 482–492 (2014).

Figures

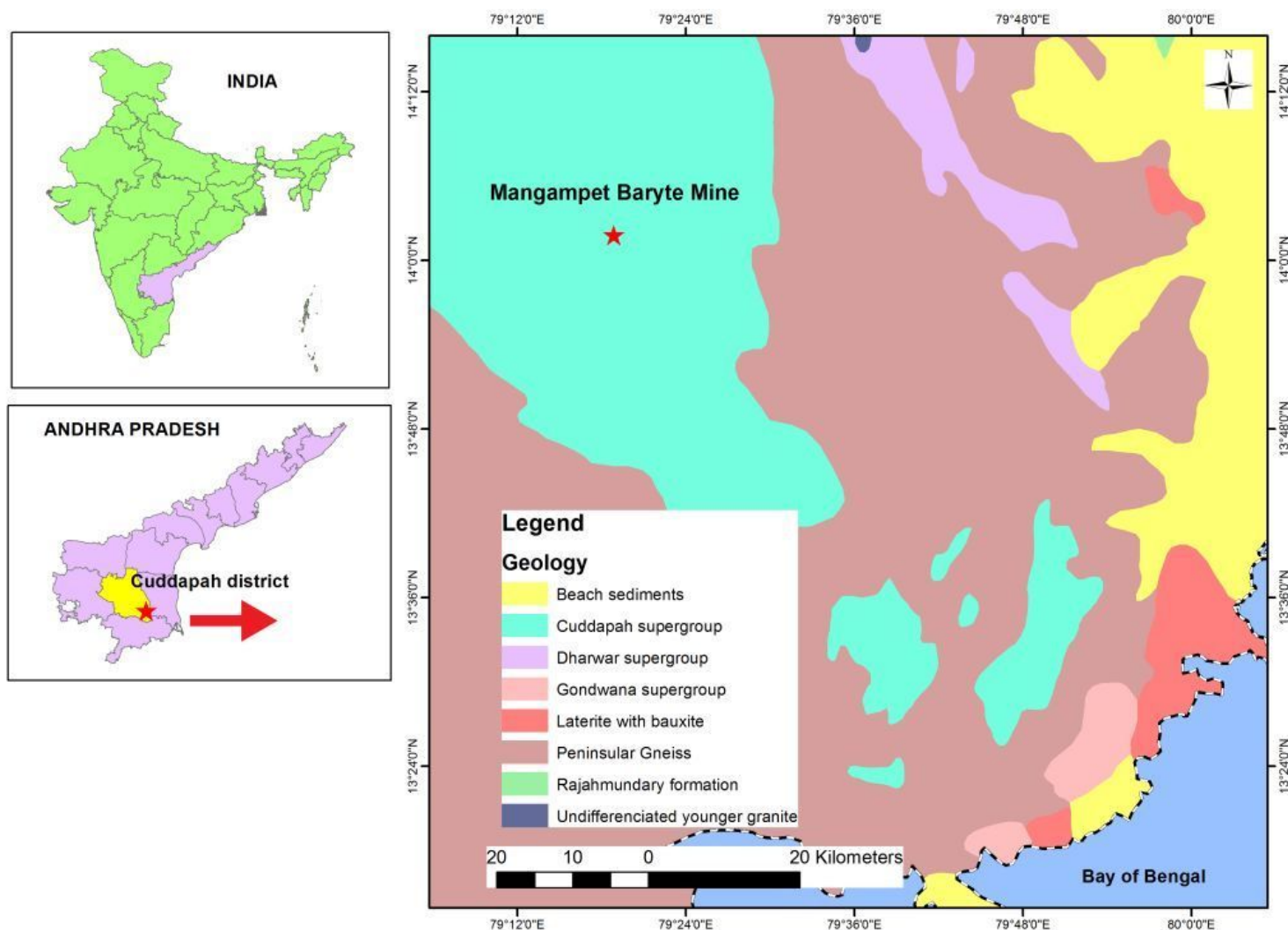


Figure 1

Study area map Note: The designations employed and the presentation of the material on this map do not imply the expression of any opinion whatsoever on the part of Research Square concerning the legal status of any country, territory, city or area or of its authorities, or concerning the delimitation of its frontiers or boundaries. This map has been provided by the authors.



Figure 2

Google earth imagery of Mangampet baryte mine. Note: The designations employed and the presentation of the material on this map do not imply the expression of any opinion whatsoever on the part of Research Square concerning the legal status of any country, territory, city or area or of its authorities, or concerning the delimitation of its frontiers or boundaries. This map has been provided by the authors.

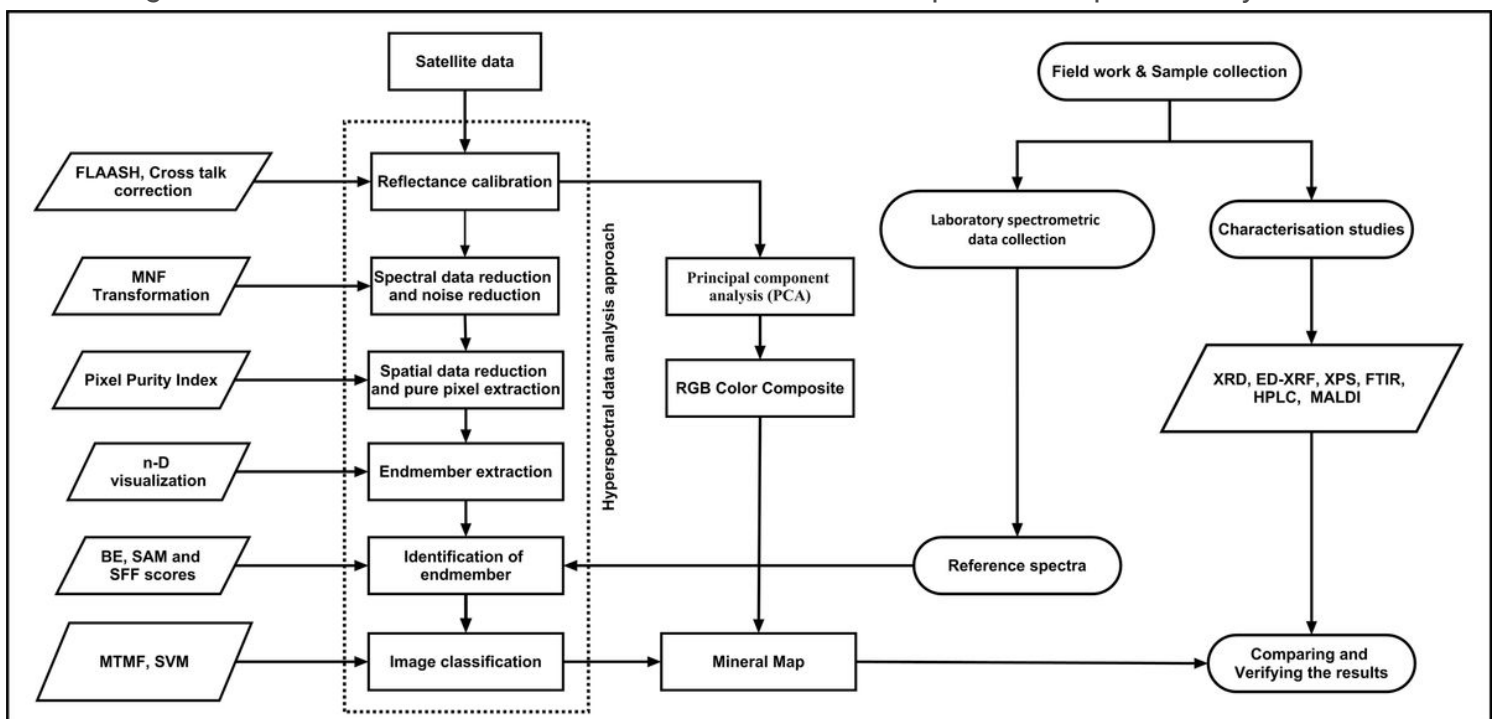


Figure 3

Flow sheet showing the methodology adopted for the present study.

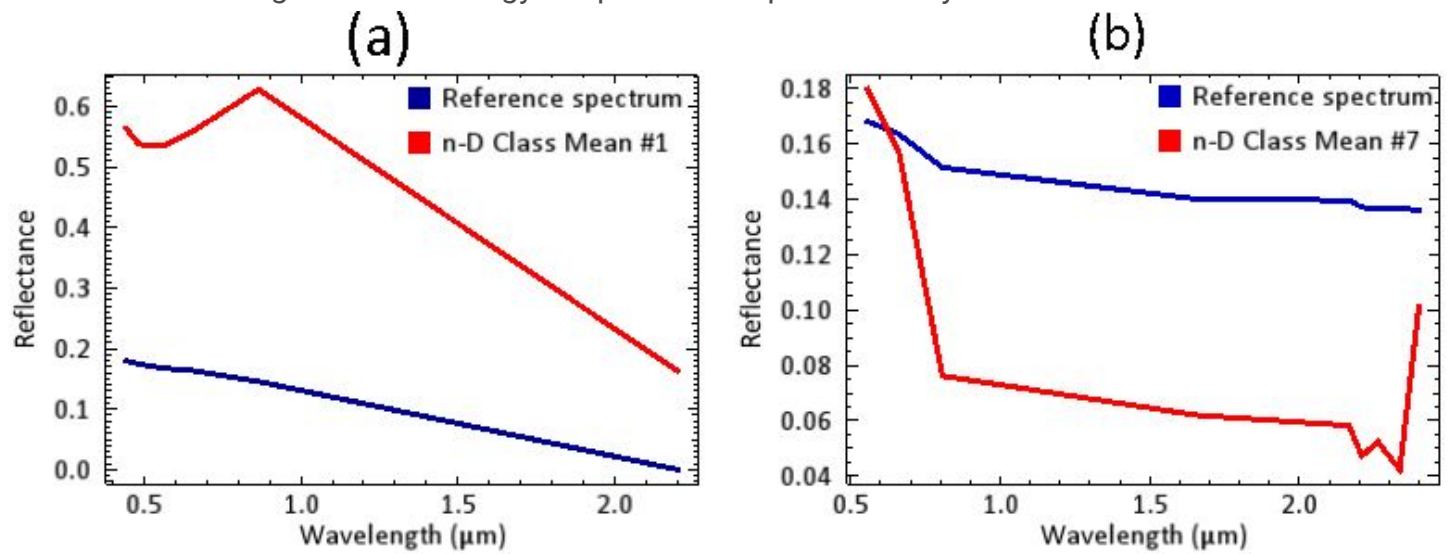


Figure 4

Plots of relative reflectance of endmember spectra and their corresponding reference spectra (a) Landsat imagery; (b) ASTER data.

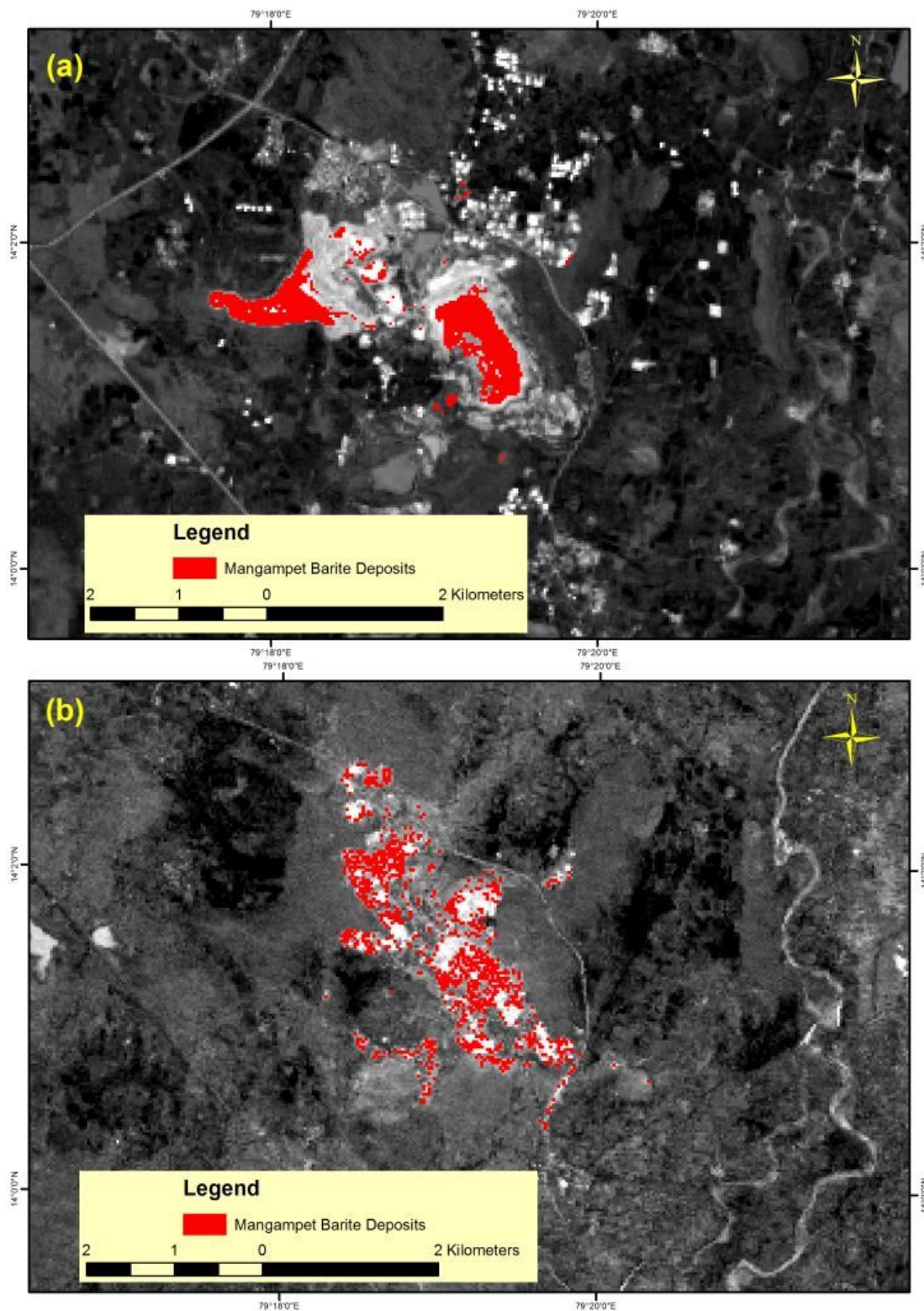


Figure 5

MTMF classified maps showing shingite rocks in mangampet mine. (a) Landsat imagery; (b) ASTER data. Note: The designations employed and the presentation of the material on this map do not imply the expression of any opinion whatsoever on the part of Research Square concerning the legal status of any country, territory, city or area or of its authorities, or concerning the delimitation of its frontiers or boundaries. This map has been provided by the authors.

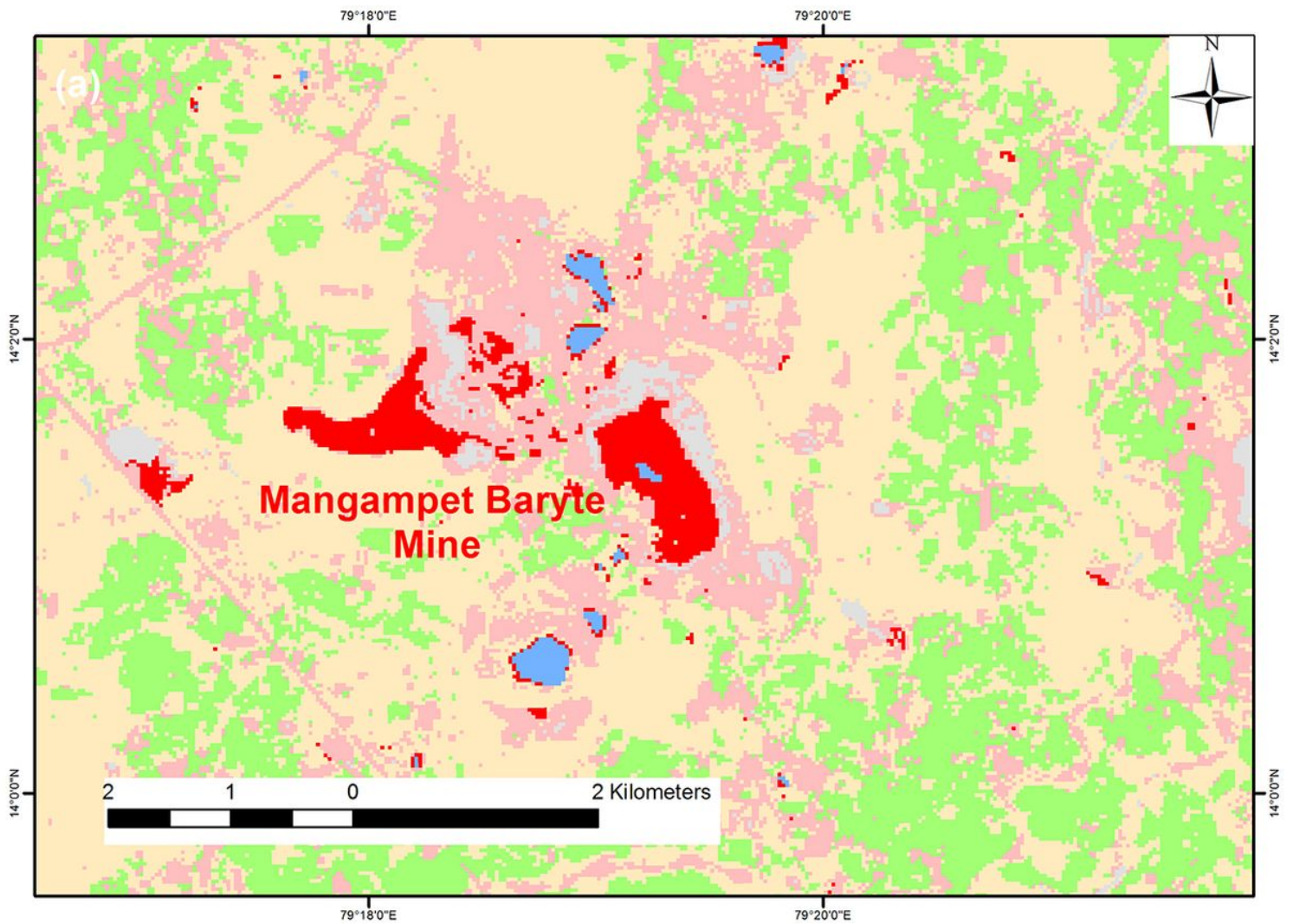


Figure 6

SVM classified image of Landsat data showing shungite rocks in red colour. Note: The designations employed and the presentation of the material on this map do not imply the expression of any opinion whatsoever on the part of Research Square concerning the legal status of any country, territory, city or area or of its authorities, or concerning the delimitation of its frontiers or boundaries. This map has been provided by the authors.

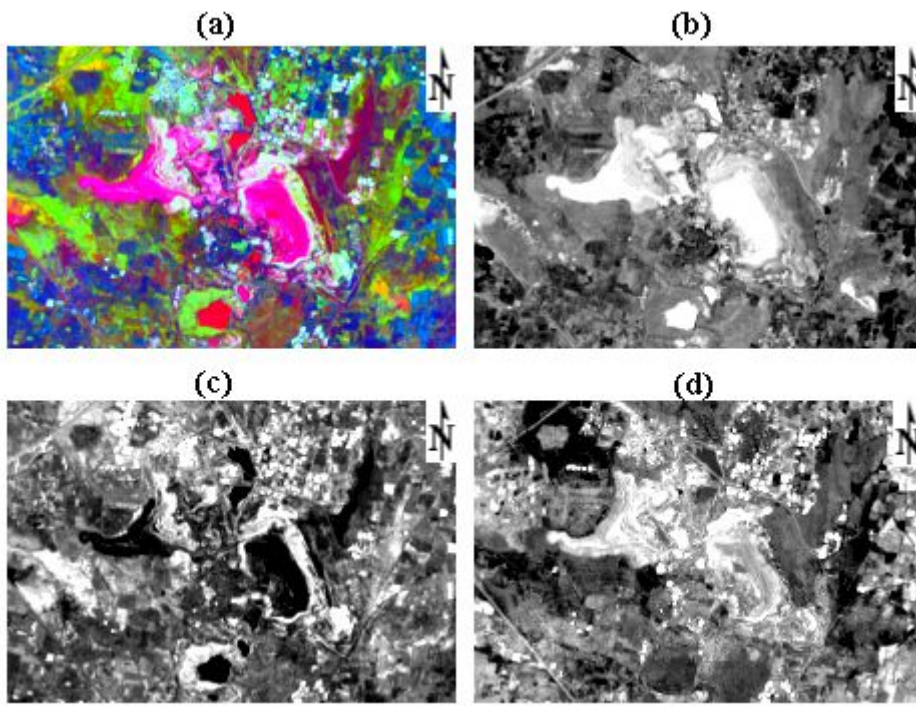


Figure 7

PCA results of Landsat data. (a) RGB color composite of PC1, PC2 and PC3; (b) PC1; (c) PC3; (d) PC3. Note: The designations employed and the presentation of the material on this map do not imply the expression of any opinion whatsoever on the part of Research Square concerning the legal status of any country, territory, city or area or of its authorities, or concerning the delimitation of its frontiers or boundaries. This map has been provided by the authors.

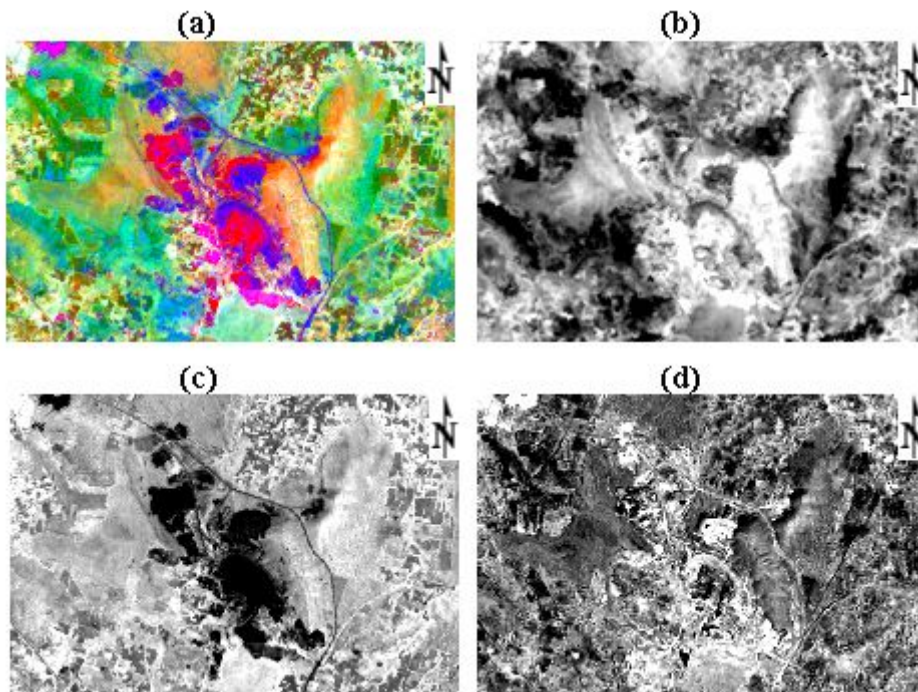


Figure 8

PCA results of ASTER data. (a) RGB color composite of PC1, PC2 and PC3; (b) PC1; (c) PC3; (d) PC3. Note: The designations employed and the presentation of the material on this map do not imply the expression of any opinion whatsoever on the part of Research Square concerning the legal status of any country, territory, city or area or of its authorities, or concerning the delimitation of its frontiers or boundaries. This map has been provided by the authors.

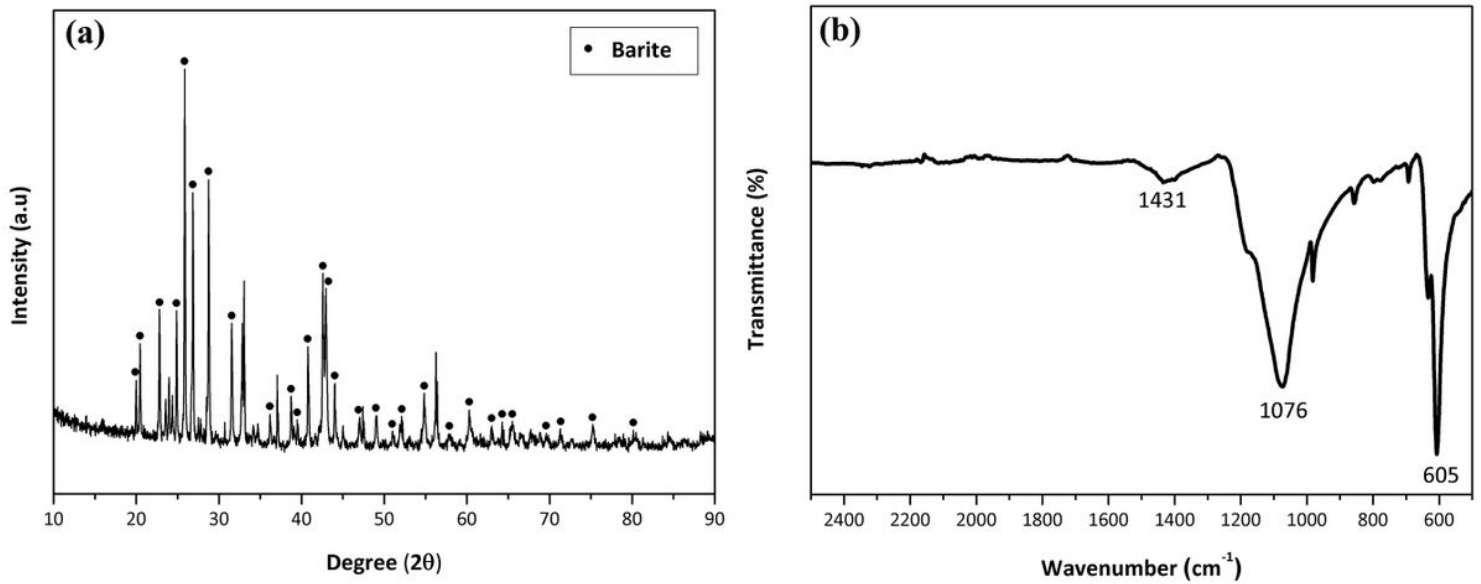


Figure 9

Characterisation results of barite. (a) XRD; (b) ATR-FTR

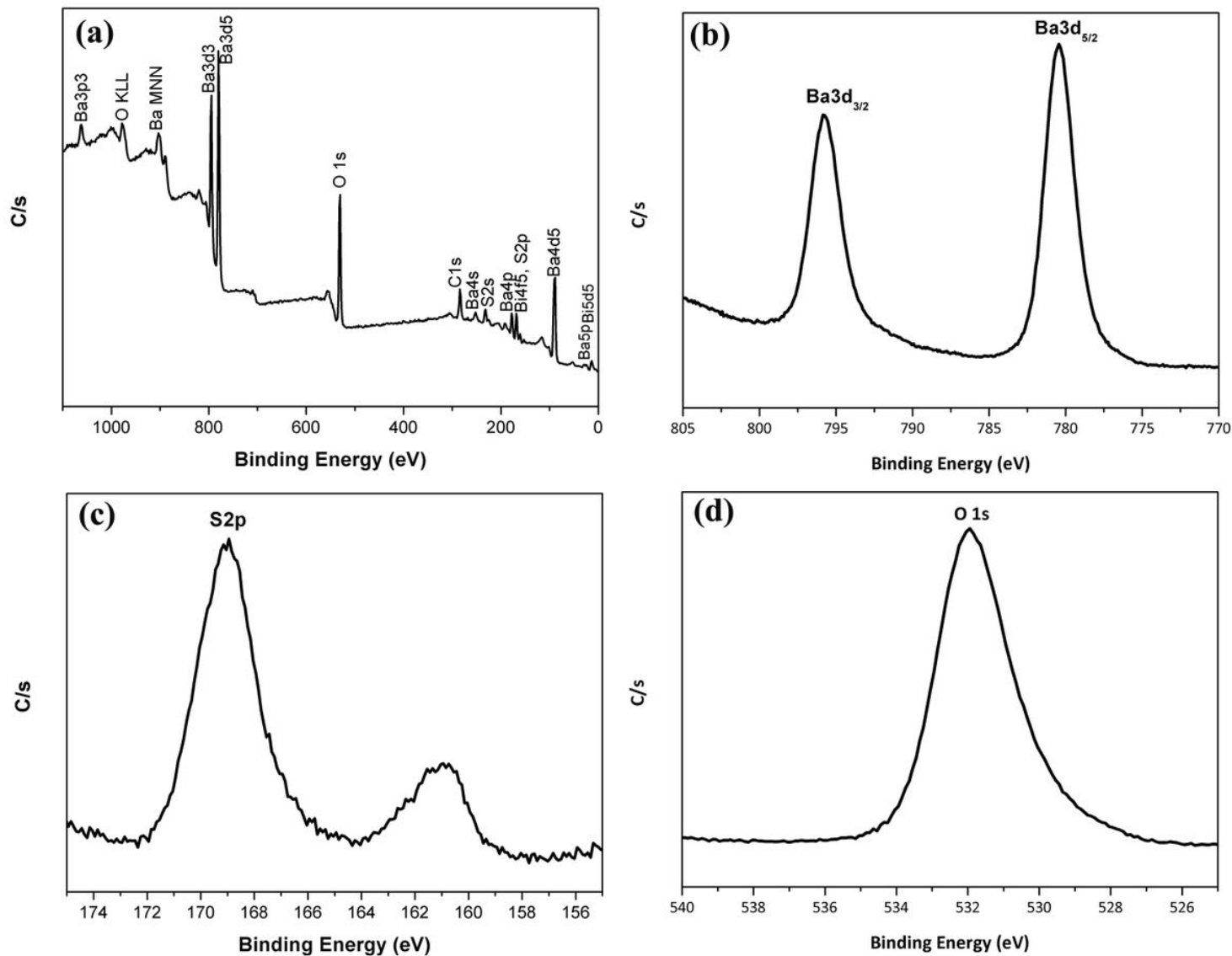


Figure 10

XPS results of barite.(a) Wide scan XPS spectra, and high resolution scans of (b) Ba3d, and (c) S2p, and (d) O1s.

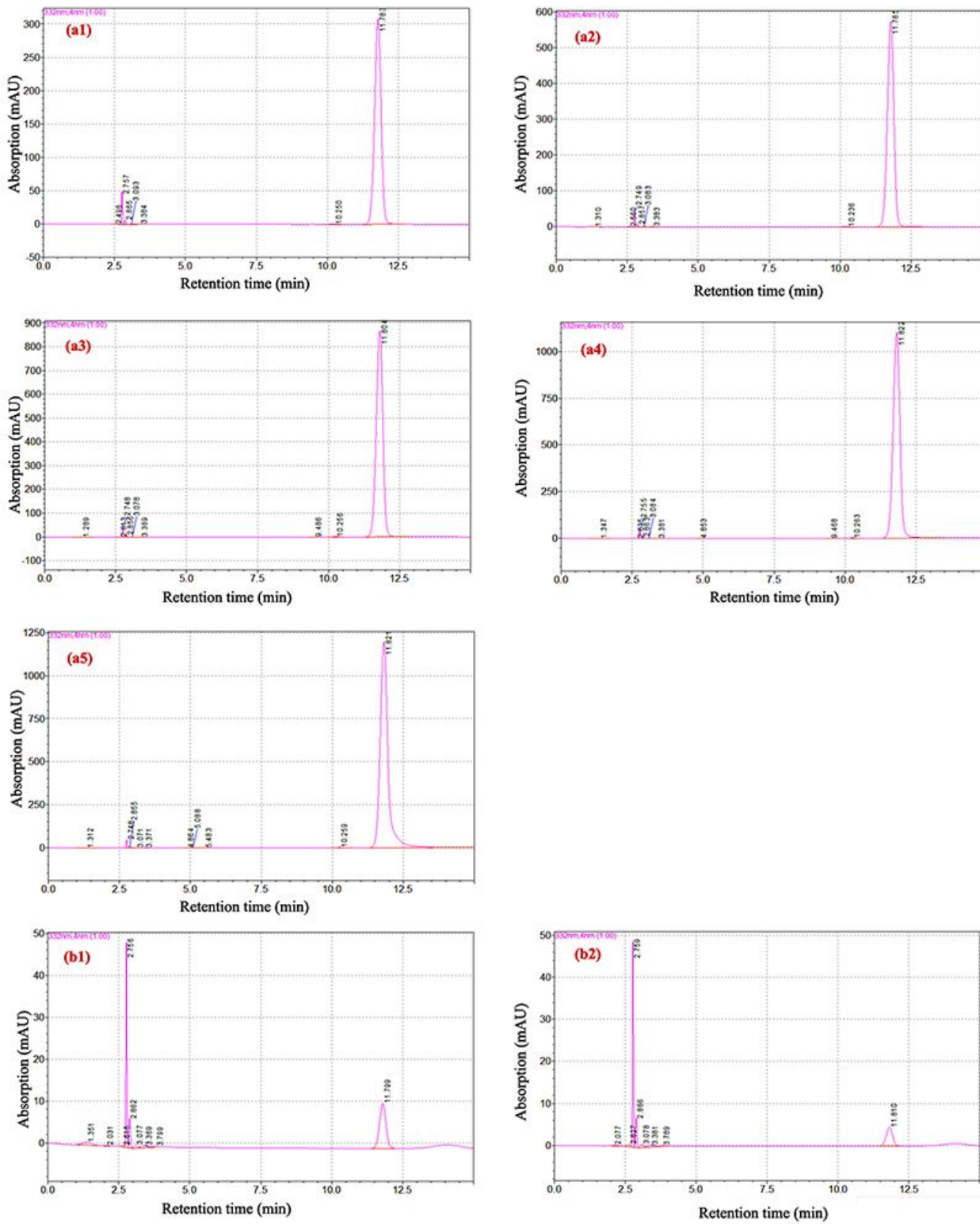


Figure 11

HPLC results. (a1-a5) Fullerene standard; (b1-b2) Barite samples.

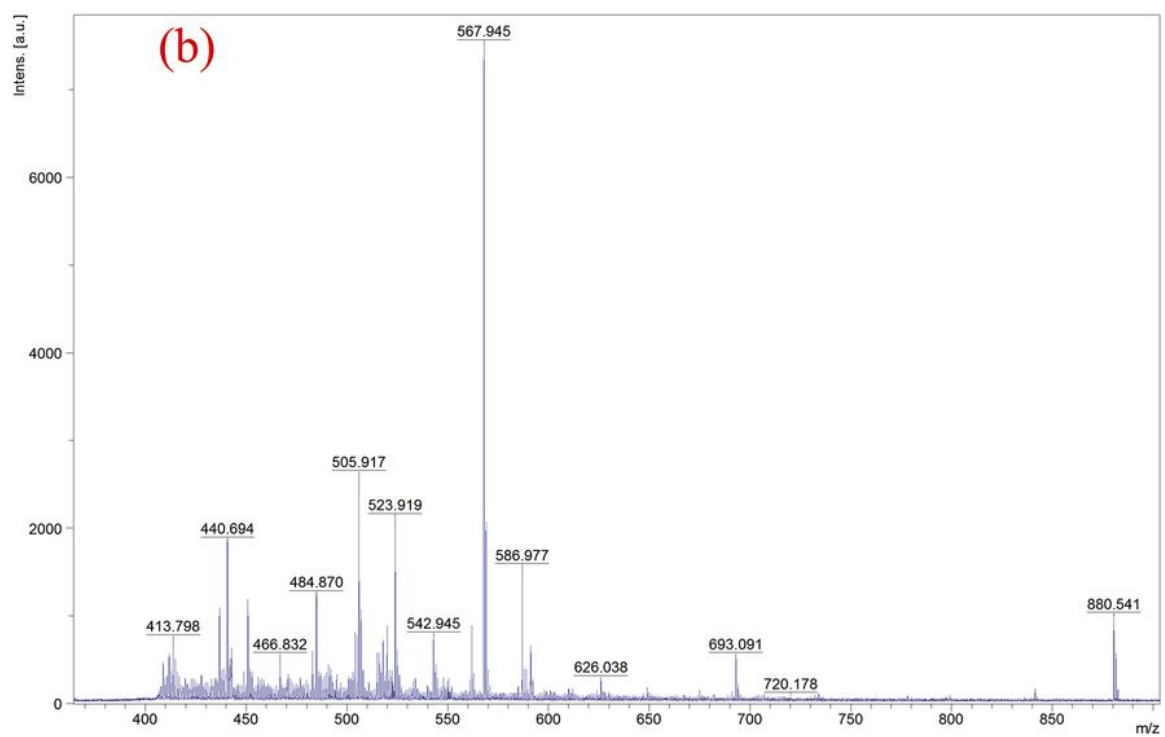
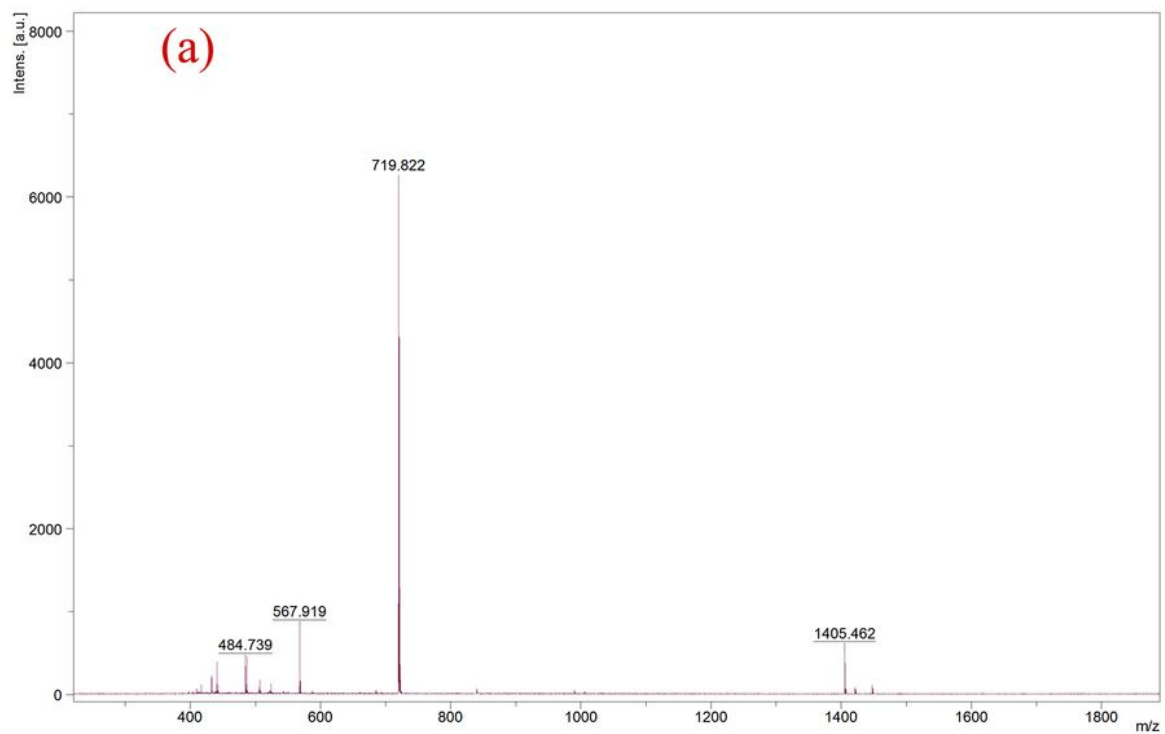


Figure 12

MALDI mass spectrum.(a) Fullerene standard; (b) barite samples.